

On backflow associated with oceanic and continental subduction

Evangelos Moulas¹, Mark T. Brandon², Joshua D. Vaughan Hammon³ and Stefan M. Schmalholz³

¹Institute of Geosciences & Mainz Institute of Multiscale Modeling (M³ODEL), Johannes-Gutenberg University, 55128 Mainz, Germany.

E-mail: evmoulas@uni-mainz.de

²Department of Earth and Planetary Sciences, Yale University, New Haven, CT 06511, USA

³Institut des sciences de la Terre, University of Lausanne, 1015 Lausanne, Switzerland

Accepted 2021 June 24. Received 2021 June 17; in original form 2020 November 30

SUMMARY

A popular idea is that accretion of sediment at a subduction zone commonly leads to the formation of a *subduction channel*, which is envisioned as a narrow zone located above a subducting plate and filled with vigorously circulating accreted sediment and exotic blocks. The circulation can be viewed as a forced convection, with downward flow in the lower part of the channel due to entrainment by the subducting plate, and a ‘backflow’ in the upper part of the channel. The backflow is often cited as an explanation for the exhumation of high-pressure/low-temperature metamorphic rocks from depths of 30 to 50 km. Previous analyses of this problem have mainly focused on the restricted case where the walls bounding the flow are artificially held fixed and rigid. A key question is if this configuration can be sustained on a geologically relevant timescale. We address this question using a coupled pair of corner flows. The *pro-corner* accounts for accretion and deformation directly above the subducting plate, and the *retro-corner* corresponds to a deformable region in the overlying plate. The two corners share a *medial boundary*, which is fully coupled but is otherwise free to rotate and deform. Our results indicate that the maintenance of a stable circulating flow in a narrow pro-corner ($<15^\circ$) requires an unusually large viscosity ratio, $\mu_{\text{retro}}/\mu_{\text{pro}} > 10^3$. For lower viscosity ratios, the medial boundary would rotate rearwards, converting the initially narrow pro-corner into an obtuse geometry. For a stable narrow corner, we show that the backflow within the corner is caused by downward convergence of the incoming flow and an associated downward increase in dynamic pressure, which reaches a maximum at the corner point. The total pressure is thus expected to be much greater than predicted using a lithostatic gradient, which means that estimates of depth from metamorphic pressure would have to be adjusted accordingly. In addition, we show that the velocity fields associated with a forced corner flow and a buoyancy-assisted channel flow are nearly identical. As such, structural geology studies are not sufficient to distinguish between these two processes.

Key words: Numerical approximations and analysis; Numerical modelling; Continental margins: convergent; Dynamics of lithosphere and mantle; Subduction zone processes.

1 INTRODUCTION

1.1 Subduction, mélanges and channel flow

The modern Earth has about 92 000 km of convergent-plate boundaries (Bird 2003). About 56 per cent of that length involves subduction of oceanic lithosphere and about 25 per cent of that length involves subduction of continental lithosphere. Continental subduction was first proposed by Ampferer & Hammer (1911) and Argand (1916, 1924) for the Alps and the Himalaya. The idea was greatly expanded during the middle 1900s with the discovery of

Wadati–Benioff zones, indicating large-scale subduction of oceanic lithosphere. We start with this history because we find it useful to use the term *subduction zone* in a generic sense to indicate a lithosphere-scale boundary where one plate is carried beneath another, regardless of the composition of the subducting plate.

A subduction zone must start with the formation of a sharp fault boundary. The subducting plate commonly includes a sedimentary cover, which can have a thickness ranging from 0 to 10 km. If present, part or all of the sedimentary cover can be carried deep into the subduction boundary. There has been much research, speculation, and debate about the deformation that occurs within this

boundary zone. Some authors favor a view that the deformation occurs mainly by thrust imbrication, and others argue for a more mobile and chaotic style of deformation, as represented by the term *mélange* (e.g. Ring & Brandon 1999; Krohe 2017). We expand on this topic because the idea of tectonic mixing has long been a motivating factor for the idea of a channel flow associated with subduction.

A *mélange* is a regional-scale mappable body, characterized by a chaotic block-and-matrix structure (Cowan 1985). In some cases, the blocks can be shown to be ‘exotic’, in that they were introduced into the matrix during the formation of the *mélange*. The classic example is the mudstone-matrix *mélanges* of the Franciscan Complex, which locally contain blueschists and eclogites with metamorphic pressure up to ~ 1.5 GPa (Wakabayashi 2015).

There has been a long debate about the origin of this deformational style. Starting in the 1970s, many geologists considered *mélanges* to be a distinctive and diagnostic feature of deformation within an active subduction zone. Many *mélanges* display a scaly foliation, which has been taken as evidence that the mixing process was associated with shearing. High pore-fluid pressures are commonly invoked as well to account for the pervasive and fluid-like mixing observed in most *mélanges*. It is useful to note that scientific drilling at modern subduction zones has yet to find an actively forming tectonic *mélange* (Lundberg & Moore 1986). Perhaps this discovery will require drilling to much greater depths than is currently possible.

An alternative interpretation is that the chaotic and highly mixed structure observed in *mélanges* was formed by mass wasting in the surface environment, rather than by tectonic processes at depth. Improvements in seafloor imaging over the last several decades have led to the recognition that mass wasting is common at subduction zones, due to the tectonically oversteepened topography above the subduction thrust (e.g. Clausmann *et al.* 2021). Mass-wasting deposits are known to commonly accumulate in trench basins and thus should be expected to be part of the sedimentary cover that is carried into the subduction zone. Relevant near-modern examples of subducted mass-wasting deposits include the Lichi *mélange* of Taiwan (Page & Suppe 1981; Chang *et al.* 2001) and the Argille Scagliose of the northern Apennines in Italy (Camerlengi & Pini 2009).

We introduce here a modified corner-flow solution, which provides a generalized framework for assessing the mechanics and evolution of a narrow shear zone filled with a weak material. However, we make no assumptions about the possibility of chaotic mixing within the zone.

1.2 Corner flow

Our study is motivated by the original corner flow model of Cloos (1982, 1984), which was proposed as an explanation for the co-occurrence of *mélange* and exotic high-pressure/low-temperature (HP/LT) blocks in the Franciscan Complex of California. Cloos envisioned that much of the Franciscan was ‘processed’ by flow within a narrow angular region, with an opening angle of about 15° , which tapers down to a corner point located at a depth of about 40 km (Fig. 1a). In his original work, Cloos (1982) coined the term ‘flow *mélange*’ to emphasize the mixing that might occur within a narrow corner flow. In that original model, the upper boundary of the proposed corner region is held fixed, and the lower boundary is assigned a downward velocity oriented parallel to the boundary and equal to the velocity of the subducting plate.

Our focus here is to investigate the mechanical conditions and the long-term stability of flow in corner regions. The *corner flow* problem is one of the few cases in fluid dynamics where the flow field can be fully specified in analytical form, in terms of velocity, stress, and pressure. Fig. 1 illustrates tectonic settings that are amenable to analysis using the corner flow solution. Many applications have emphasized the velocity field but we show the significance of the pressure and stress field as well. Given Cloos’ boundary conditions (1982; see also Fig. 1a), the material in the lower part of the corner is entrained downward with the subducting plate, but the convergence of flow within the narrow corner causes the flow to reverse and ascend within the upper part of the corner. Cloos (1982, 1984) argued that this *backflow* was responsible for carrying HP/LT metamorphic blocks of the Franciscan Complex back to the surface. As a result, Cloos (1982, 1984) viewed Franciscan *mélanges* to be diagnostic of the mixing associated with corner flow.

England & Holland (1979) had already proposed a similar model for the exhumation of HP/LT metamorphic rocks in the Austrian Alps. Their model involved a channel parallel to the subducting plate and extending to depths of ~ 50 km, where the Austrian eclogites were thought to have originated. The low-density materials inside the channel are entrained downward with the subducting plate, which results in backflow within the upper part of the channel caused by positive buoyancy relative to the surrounding crust and mantle. In contrast, the backflow associated with the classic corner flow model is entirely driven by boundary velocities and buoyancy effects are notably ignored.

Shreve & Cloos (1986) and Cloos & Shreve (1988a,b) modified the original corner flow idea to account for a more arbitrary channel/corner geometry, and to include buoyancy forces as well. The term *subduction channel* was coined by Cloos & Shreve (1988a,b), and that term is now widely used in the literature. More recent studies have considered the effects of inclined and/or deformable walls (Mancktelow 1995; Raimbourg & Kimura 2008). Our analysis includes these possibilities.

The concept of a subduction channel was further advanced by numerical modeling. In particular, Gerya *et al.* (2002) created a detailed simulation of a narrow channel with a circulating flow, extending to depths of ~ 50 km and in some cases even 100 km. The internal geometry and rheologies used in their study were selected to match a ‘consensus view’ of what a subduction zone might look like. The two-way flow was once again envisioned as a possible mechanism for returning HP/LT metamorphic rocks back to the surface. Their simulations included cases where the flow field developed local vortices, but this result was not an emergent feature of the simulation, but instead was imposed by placement of a large re-entrant into the upper boundary of the channel.

As highlighted by Mancktelow (1995), the subduction-channel model can be viewed as a corner flow with a very narrow opening angle. At the other extreme, the wedge models of Cowan & Silling (1978), Willett *et al.* (1993), Beaumont & Quinlan (1994) and Jamieson & Beaumont (2013) can be viewed as corner flows with very large opening angles. Cowan & Silling (1978) demonstrated this point by showing the similarity of the velocity field observed in their scaled analogue model of a wedge with a 90° corner geometry, and that for a corner flow with the same velocity boundaries and a 90° geometry.

We consider the corner-flow solution as providing a general mechanical representation of a wide range of models, from channels, narrow corners and wide wedges. Our analysis here is based on two-corner flows that are coupled across a common medial boundary

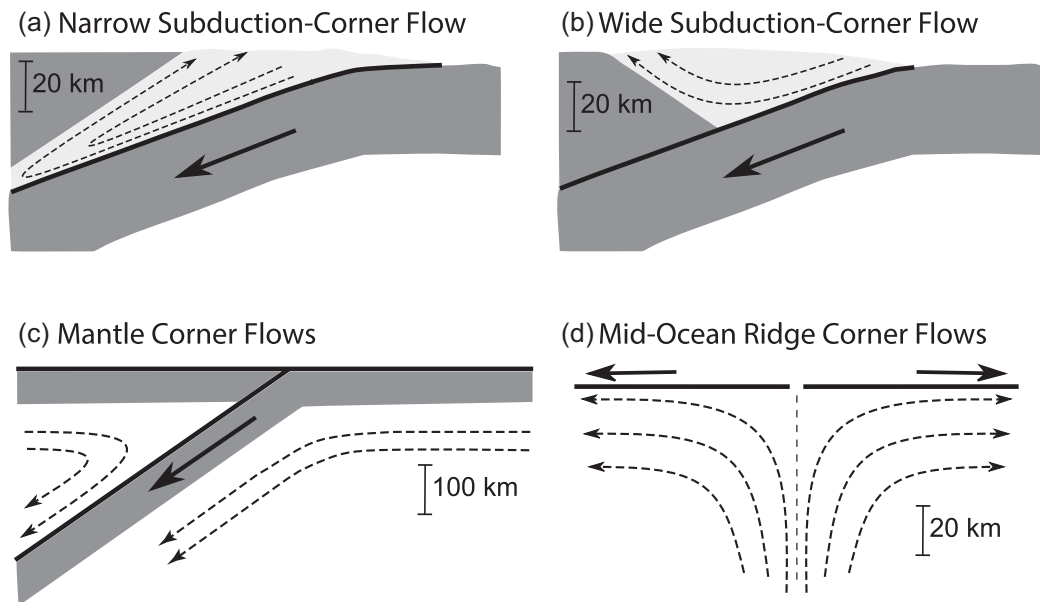


Figure 1. Schematic geometries that illustrate the essential parts of various corner-flow models (modified after Tovish *et al.* 1978; Cloos 1982; Spiegelman & McKenzie 1987; Willett *et al.* 1993). The dark grey regions depict rigid plates. The dashed arrows indicate flow lines. The scales are approximate and the sections have no vertical exaggeration.

(Fig. 2). The *pro-corner* is equivalent to the channel/corner discussed above. The *retro-corner* lies rearward of the pro-corner, and corresponds to what many authors would call the ‘upper plate’. Note however that the introduction of a retro-corner allows this ‘upper plate’ region to deform if the loads become large enough. The pro- and retro-corners have different viscosities, as represented by μ_1 and μ_2 , respectively. Following the notation as shown in Fig. 2, the corner point is designated by an ‘S’, which highlights the fact that the boundary conditions are the same as the S-point boundary condition introduced by Willett *et al.* (1993), and Beaumont & Quinlan (1994). Following their convention, the retro-boundary is assigned to the Moho in the overriding plate. This decision accounts for the fact that the upper-plate mantle that underlies this boundary should be much stronger (higher viscosity) than the overlying crust. Thus θ_2 is set to 150° , which implies that the subducting plate dips at 30° relative to a horizontal upper-plate Moho. The pro- and retro-boundaries are held fixed in space, and are assigned uniform velocities \vec{V}_0 and \vec{V}_2 (Fig. 2). For the analysis here, the retro-boundary is assigned a zero velocity ($\vec{V}_2 = \vec{0}$, i.e. no slip on the boundary), but the retro-corner is otherwise free to deform internally. The velocities are all specified relative to a fixed corner (S-point fixed reference frame). The velocity on the pro-boundary accounts for entrainment and basal accretion, as represented by the radial and circumferential components of \vec{V}_0 relative to the pro-boundary. For simplicity, we focus exclusively on the case of entrainment, which means that \vec{V}_0 is parallel to the pro-boundary and $|\vec{V}_0| = -U$.

In previous corner-flow models, the parameter U was often assumed to be equal to the velocity of the subducting plate, but this assumption overlooks the fact that discrete slip on the subduction thrust accounts for much of the subduction velocity. For the Cascadia subduction zone, Pazzaglia & Brandon (2001) showed that the long-term velocities at the base of the Cascadia wedge in Washington State are about an order of magnitude smaller than the subduction velocity. Thus, for a typical subduction velocity of $\sim 50 \text{ mm a}^{-1}$, we might expect an entrainment velocity $U \approx 5 \text{ mm a}^{-1}$. Note that

if the pro-boundary were fully decoupled from the subducting plate, then $U = 0$ and there would be no flow within the pro-corner.

1.3 Organization of the paper

The paper is organized into three parts. The first part reviews solutions for a single corner (Section 2.1) and shows the derivation of an analytical solution for coupled corner flows (Section 2.2). In addition, we describe a numerical method that we use for comparison with the analytical approach (Section 2.3). In the second part (Sections 3.1 and 3.2), we present results from the analytical two-corner solution to assess the conditions necessary for maintenance of a stable corner geometry. We focus on the backflow, as this part of the flow field is thought to be important for exhumation of HP/LT rocks. Our results show that, for narrow corners where the backflow is strongest, the dynamic pressure within the corner is typically of the same order as the lithostatic pressure. The third part uses numerical results (Section 3.3) to understand the rate at which the pro-corner evolves towards a stable geometry. We finish with a discussion regarding the implications of our results for structural and metamorphic studies of subduction zones.

2 METHODS

2.1 Analytical solutions for corner flow in geodynamics

Analytical models provide a way to reduce a problem to a simpler form and a smaller set of controlling variables (e.g. Fletcher 1977; Emerman & Turcotte 1983; Medvedev 2002; Schmalholz 2011; Ribe & Xu 2020). Corner-flow solutions have been widely used in geodynamics, with applications to orogenic wedges (Figs 1a and b; Cowan & Silling 1978; Cloos 1982), and for the study of mantle flow associated with subduction (Fig. 1c; Stevenson & Turner 1977; Tovish *et al.* 1978), spreading centers (Fig. 1d; McKenzie 1969; Spiegelman & McKenzie 1987), and backarc spreading (Ribe 1989).

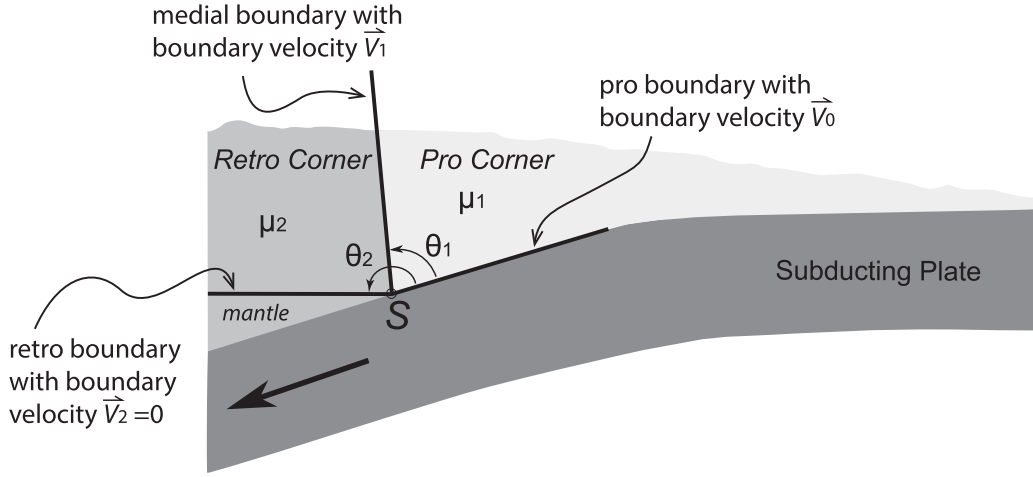


Figure 2. Schematic illustration of two coupled corner flows. The pro-corner is equivalent to the ‘subduction corner’ or ‘subduction channel’ considered in previous models. The retro-corner represents a deformable region within the overriding plate. This configuration allows us to test the long-term stability of the pro-corner. The pro- and retro-corners are assigned different viscosities μ_1 and μ_2 , respectively, where $\mu_2 > \mu_1$.

In our opinion, Batchelor (1967), Dean & Montagnon (1949), McKenzie (1969) and Moffatt (1964) provide good introductions to this topic. These papers generally focus on the simple case where the material in the corner has a uniform viscosity, and one of the boundaries has uniform circumferential velocity and the other boundary is stationary. However, the corner-flow problem has been extended to include more complex boundary conditions (Moffatt 1964; Sprittles & Shikhmurzaev 2011), more complex configurations (coupled corner flows: Anderson & Davis 1993; leaky corner: Rieder & Schneider 1983) and nonlinear rheologies (Tovish *et al.* 1978; Riedler & Schneider 1983; Henriksen & Hassager 1989; Ribe 2015, 2018). This last development is important because it has shown that the kinematics of a corner flow are relatively insensitive to the specifics of the rheology. In fact, the assumption of constant viscosity is common invoked in studies of subduction zones, shear zones, wedges, glaciers, and mantle convection (e.g. McKenzie 1969; Spiegelman & McKenzie 1987; England & Wilkins 2004; Pollard & Fletcher 2005; Moulas *et al.* 2014). Based on this background, we too have decided that constant viscosity is an appropriate approximation for a first-order analysis of corner flow. Of course, numerical methods allow the use of more realistic rheologies, and this capability may be useful for situations where simulations can be directly compared with observations.

2.2 Analytical solution for the two-corner region

Herein, we develop a two-corner solution for our analysis of corner flow in subduction zones. Anderson & Davis (1993) provide a general development of two-corner solutions as relevant to fluid dynamics.

The stream function ψ provides a method for setting up a general solution for a slow incompressible viscous flow (i.e. Stokes flow) in a single corner. The stream function can be written in polar coordinates as

$$\psi(r, \theta) = r f(\theta), \quad (1)$$

where r is the radial coordinate and θ is the angular coordinate relative to the corner point. The function $f(\theta)$ is selected so that the stream function satisfies the biharmonic equation, $\nabla^4 \psi(r, \theta) = 0$, which ensures a full solution for velocities and stresses inside the corner region and extending to $r = +\infty$. For the classic corner-flow

solution with kinematic boundary conditions, the angular function in eq. (1) has the general form

$$f(\theta) = A \cos(\theta) + B \sin(\theta) + C \theta \cos(\theta) + D \theta \sin(\theta). \quad (2)$$

The constants A, B, C, D are determined by setting constant velocities on each of the two boundaries of the corner, located at θ_0 and θ_1 . The two velocity components for each of the two boundaries means that there are four boundary equations, which are solved to get the four unknown constants A, B, C, D . Velocities and stress components for the flow field inside the corner are obtained by differentiation of the stream function (c.f., McKenzie 1969, p. 15–16). The radial V_r and circumferential V_θ components of the velocities are given by

$$V_r = \frac{1}{r} \frac{\partial \psi}{\partial \theta}, \quad V_\theta = -\frac{\partial \psi}{\partial r}, \quad (3)$$

where a positive radial velocity indicates motion outward from the corner, and a positive circumferential velocity indicates a counter-clockwise motion.

The components of the deviatoric stress tensor τ_{ij} in polar coordinates are given by

$$\tau_{rr} = 2\mu_k \frac{\partial V_r}{\partial r}, \quad (4a)$$

$$\tau_{\theta\theta} = 2\mu_k \left(\frac{1}{r} \frac{\partial V_\theta}{\partial \theta} + \frac{V_r}{r} \right), \quad (4b)$$

and

$$\tau_{r\theta} = \mu_k \left(\frac{1}{r} \frac{\partial V_r}{\partial \theta} + \frac{\partial V_\theta}{\partial r} - \frac{V_\theta}{r} \right), \quad (4c)$$

where μ_k is the dynamic viscosity and the subscript k is used to designate between two corners. For the single corner case discussed here, $k = 1$.

The radial symmetry of the corner flow indicates that normal deviatoric stresses, τ_{rr} and $\tau_{\theta\theta}$, are identically zero, which means that $\tau_{r\theta}$ is the only non-zero component of the deviatoric stress tensor (McKenzie 1969, p. 15; Tovish *et al.* 1978). The total stress tensor σ_{ij} is related to the deviatoric stress tensor τ_{ij} by

$$\sigma_{ij} = -P \delta_{ij} + \tau_{ij}, \quad (5)$$

which indicates that the total pressure P is equal to the negative mean stress (δ_{ij} is the Kronecker delta). The total pressure P is the

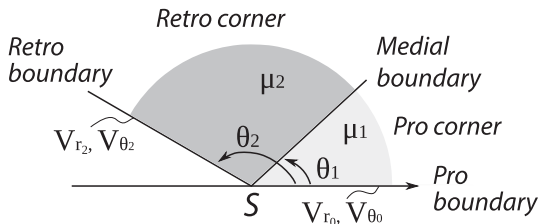


Figure 3. Convention used for two-corner flow problem. The corner regions require specification of uniform velocity components (V_r , V_θ) in the radial and circumferential directions for each boundary.

sum of the static pressure P_s , which is defined as the pressure in the static state (i.e. zero flow), and the dynamic pressure P_d , which is associated with an active flow. In geodynamics, $P_s = \rho g z$ where ρ is the density, g is the gravitational acceleration, and z is depth relative to the Earth's surface. Small corrections to this formula apply in the case where the material is compressible and where the pressure at the surface is not exactly zero (e.g. Moulas *et al.* 2019). Note that the corner-flow solution is dependent on P_d , but is entirely independent on P_s . The dynamic pressure P_d is determined by integrating the following stress-equilibrium equation,

$$-\frac{\partial P_d}{\partial r} + \frac{1}{r} \frac{\partial \tau_{r\theta}}{\partial \theta} = 0, \quad (6)$$

in the radial direction (e.g. Tovish *et al.* 1978).

Our discussion of results is assisted by normalizing (or ‘non-dimensionalizing’) field variables relative to characteristic values for the subduction problem. Velocities are normalized by the entrainment velocity at the base of a typical accreting subduction wedge, which we estimate to be $U_c \approx 5 \text{ mm a}^{-1}$. Note that the radial velocity component, V_{r0} , at the base of the pro-corner becomes $V_{r0}/U_c = -1$ when converted into a non-dimensional form. The negative indicates that entrainment draws material downwards to the corner point. Given the radial geometry of the corner-flow problem, there is no characteristic length-scale. Thus, we select a length-scale, $L_c = 10 \text{ km}$, that is representative of the region of interest adjacent to the corner point. A characteristic timescale for flow in the vicinity of the corner point is given by $t_c = L_c/U_c = 2 \text{ Ma}$. The characteristic viscosity is set to $\mu_c = 10^{19} \text{ Pa s}$, which is about 100 times less than the viscosity of the upper mantle ($\sim 10^{21} \text{ Pa s}$). All stresses and pressure are normalized by the characteristic viscous shear stress, which is defined by $\tau_c = \mu_c U_c / L_c \approx 0.16 \text{ MPa}$. Note that the solution for the velocity field in a corner flow problem does not require specification of a viscosity. Viscosity is only needed when calculating stresses and pressure. In addition, the non-dimensional approach ensures that our stress and pressures are only sensitive to the relative variation in viscosity, not the absolute values.

The two-corner problem (Fig. 3) is solved using two coupled stream functions,

$$\psi_k(r, \theta) = r (A_k \cos(\theta) + B_k \sin(\theta) + C_k \theta \cos(\theta) + D_k \theta \sin(\theta)), \quad (7)$$

where the subscript $k = 1, 2$, representing the pro- and retro-corners, respectively. The paired stream functions now contain eight unknown constants, A_k, B_k, C_k, D_k with k accounting for the two corners. The boundary conditions provide eight equations, which are used to solve for these constants. Four of these equations are:

$$V_r(r, \theta_0) = V_{r0}, \quad (8a)$$

$$V_\theta(r, \theta_0) = V_{\theta0}, \quad (8b)$$

$$V_r(r, \theta_2) = V_{r2}, \quad (8c)$$

and

$$V_\theta(r, \theta_2) = V_{\theta2}. \quad (8d)$$

For the remaining four equations, we consider the continuity of velocity and traction along the medial boundary, $\theta = \theta_1$. However, since $\tau_{rr} = \tau_{\theta\theta} = 0$, the total stress components normal to the medial boundary are equal to P_d . Therefore, the continuity of velocity and the stress balance at the medial boundary provides the remaining four equations, and they reduce to

$$V_r(r, \theta_1)^{\text{retro}} = V_r(r, \theta_1)^{\text{pro}}, \quad (9a)$$

$$V_\theta(r, \theta_1)^{\text{retro}} = V_\theta(r, \theta_1)^{\text{pro}}, \quad (9b)$$

$$P_d(r, \theta_1)^{\text{retro}} = P_d(r, \theta_1)^{\text{pro}}, \quad (9c)$$

and

$$\tau_{r\theta}(r, \theta_1)^{\text{retro}} = \tau_{r\theta}(r, \theta_1)^{\text{pro}}. \quad (9d)$$

The medial boundary is marked by a discontinuity in viscosity, and typically this would cause a discontinuity in the P_d field. However, the derivation above shows that the two-corner problem is special in that the P_d field is continuous across the medial boundary, as concluded by eq. (9c).

The polar velocity coordinates can be converted into Cartesian coordinates using the following transformation:

$$V_x = V_r \cos(\theta) - V_\theta \sin(\theta), \quad (10a)$$

and

$$V_y = V_r \sin(\theta) + V_\theta \cos(\theta), \quad (10b)$$

where x and y are oriented at $\theta = 0^\circ$ and 90° , respectively.

The electronic supplement contains a computer-algebra (wxMaxima) script that was used to find the analytical solution for the eight unknown constants, and two MATLAB programs that were used to calculate and visualize the full analytical solution.

2.3 Numerical calculations

We compare our analytical two-corner solution with numerical solutions produced by the open-source finite-difference code M2Di (Räss *et al.* 2017), which solves the incompressible Stokes equations using finite difference on a staggered grid. M2Di has been extensively benchmarked and tested for problems that involve viscosity discontinuities, folding/necking instabilities, and general geodynamic calculations (Schmid & Podladchikov 2003; Adamuszek *et al.* 2016).

One common problem with numerical modeling is the inability of the mesh to remain conformal with material interfaces, which causes discretization errors. This problem can be treated by increasing the grid resolution as shown in Fig. 4(a). In addition, we have added a semi-Lagrangian, backward-characteristic method (*cf.* Beuchert & Podladchikov 2010) to M2Di to ensure better performance with advection of material. This approach has been tested in cases of folding in the presence of heterogeneities for large strains (Moulas & Schmalholz 2020).

The numerical solutions were run with the two-corner problem set to $\theta_2 = 180^\circ$, which provides an easier geometry for implementing the boundary conditions. Fig. 4 shows benchmark comparisons of the numerical solutions. For these cases, we used a square domain and applied boundary velocities determined from the analytical solution. Figs 4(b) and (c) shows that the P_d field calculated by the

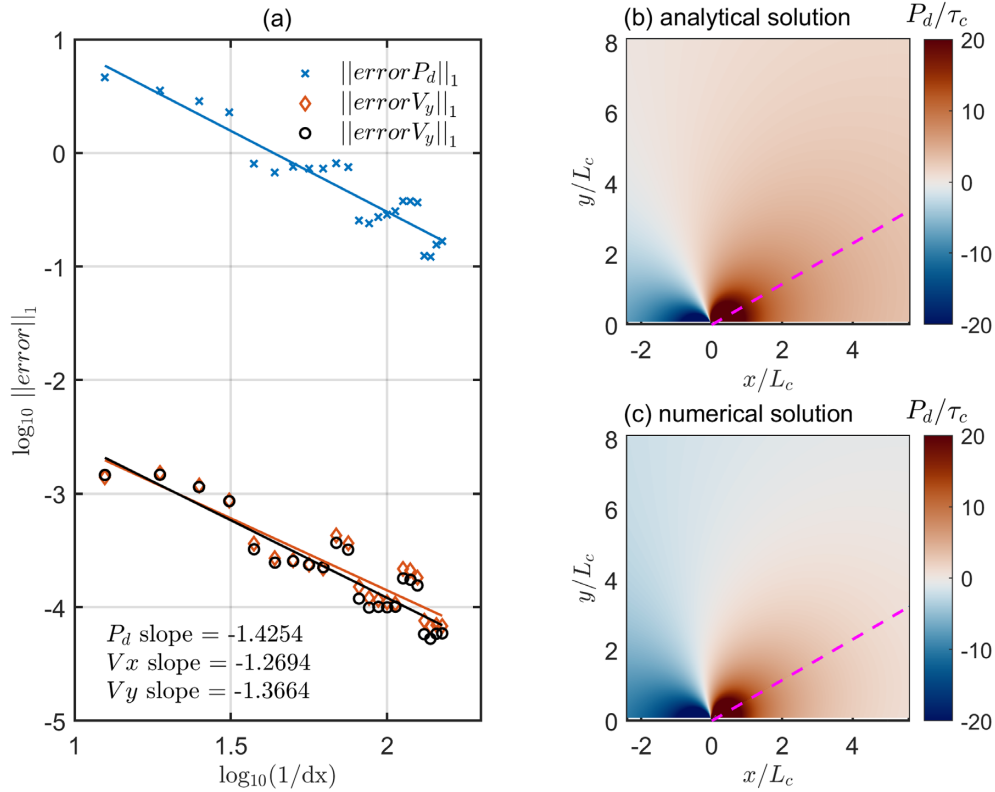


Figure 4. Comparison of analytical and numerical solutions for a pro-corner with opening angle of 30° and $\frac{\mu_2}{\mu_1} = 10^3$. The remaining parameters are $\theta_0 = 0$, $\theta_2 = 180^\circ$, $V_{r_0} = -1$, $V_{\theta_0} = 0$, $V_{r_2} = 0$, $V_{\theta_2} = 0$. (a) Error for dynamic pressure P_d , and the horizontal V_x and the vertical V_y velocity components plotted as a function of the uniform grid increment ($1/dx$). The solid lines indicate linear fits to the actual numerical results (indicated by symbols) and they show that the results are ~ 1 order of magnitude more precise for an order of magnitude greater spatial resolution. The error is the average of the absolute difference between the analytical and the numerical solutions for the square domain shown in the right panels. See Duretz *et al.* (2011) and Räss *et al.* (2017) for more details about error analysis. Comparison of (b) analytical and (c) numerical solutions show that the P_d fields around the corner are match closely and are continuous across the medial boundary, which is indicated by the magenta dashed line.

numerical method is very similar to that given by the analytical solution. Other observations that support the success of the numerical method are that the P_d field is continuous across the medial boundary, as required by eq. (9c), and varies smoothly around the corner point, which is a singularity and thus a potential source of numerical instability.

Later in the paper, we use the numerical method to evaluate the time evolution of the medial boundary. For those cases, the numerical domain is rectangular, with free-slip conditions for all sides except for the bottom side ($y = 0$) where a Dirichlet condition is used, with a constant horizontal velocity used for $x > 0$ and zero horizontal velocity for $x \leq 0$, and zero vertical velocity for all x .

3 RESULTS

3.1 Flow patterns as a function of geometry and viscosity ratio

The predicted flow pattern is fully defined by the location of the pro, medial and retro boundaries at θ_0 , θ_1 , θ_2 ; the boundary velocity components V_{r_0} , V_{θ_0} , V_{r_2} , V_{θ_2} ; and the viscosity ratio between the two regions μ_2/μ_1 . For the subduction problem, all of the boundary velocity components are set to zero, except for $V_{r_0} = -U$, which accounts for entrainment above the subduction thrust (Fig. 2). The geometry of the subduction zone relative to the upper-plate Moho

is set to $\theta_2 = 150^\circ$ (i.e. a subduction zone with a 30° dip passing beneath a flat upper-plate Moho). We now consider how the velocity field changes as a function of the orientation of the medial boundary, and the viscosity ratio, over the range $\mu_2/\mu_1 = 1$ to 10^3 (Figs 5–7).

We start with the case where the pro-corner has an acute opening angle ($\theta_1 = 30^\circ$) with μ_2/μ_1 increasing from 1 to 10^3 . (Note that $\mu_2/\mu_1 = 1$ is equivalent to a solution for a single corner, given that $\mu_2 = \mu_1$.) The resulting velocity fields show a gradual transition from a single obtuse corner flow when $\mu_2/\mu_1 = 1$ (Fig. 5a) to a single acute corner flow as $\mu_2/\mu_1 \rightarrow \infty$ (Fig. 5d). However, when μ_2/μ_1 is small, the velocity vectors adjacent to the medial boundary are generally oblique to that boundary, which means that the boundary will migrate rearward with time. In turn, Fig. 5(d) shows that when μ_2/μ_1 is sufficient large, the medial boundary becomes approximately stable, in that the flow no longer crosses the medial boundary. This simple observation leads to one of our main conclusions, that an acute pro-corner can only be sustained when there is a very large viscosity ratio, such as $\mu_2/\mu_1 > 1000$. For comparison, consider that the viscosity ratio for a subducting slab relative to the upper mantle is estimated to be less than 1000, and most likely in the range of 100–300 (Schellart 2008).

We now consider the case (Fig. 6) where the pro-corner has an obtuse opening angle ($\theta_1 = 130^\circ$). The examples show the same range in μ_2/μ_1 , from 1 to 10^3 . Note that for the smallest viscosity ratio (Fig. 6a), the velocities decrease to very small values

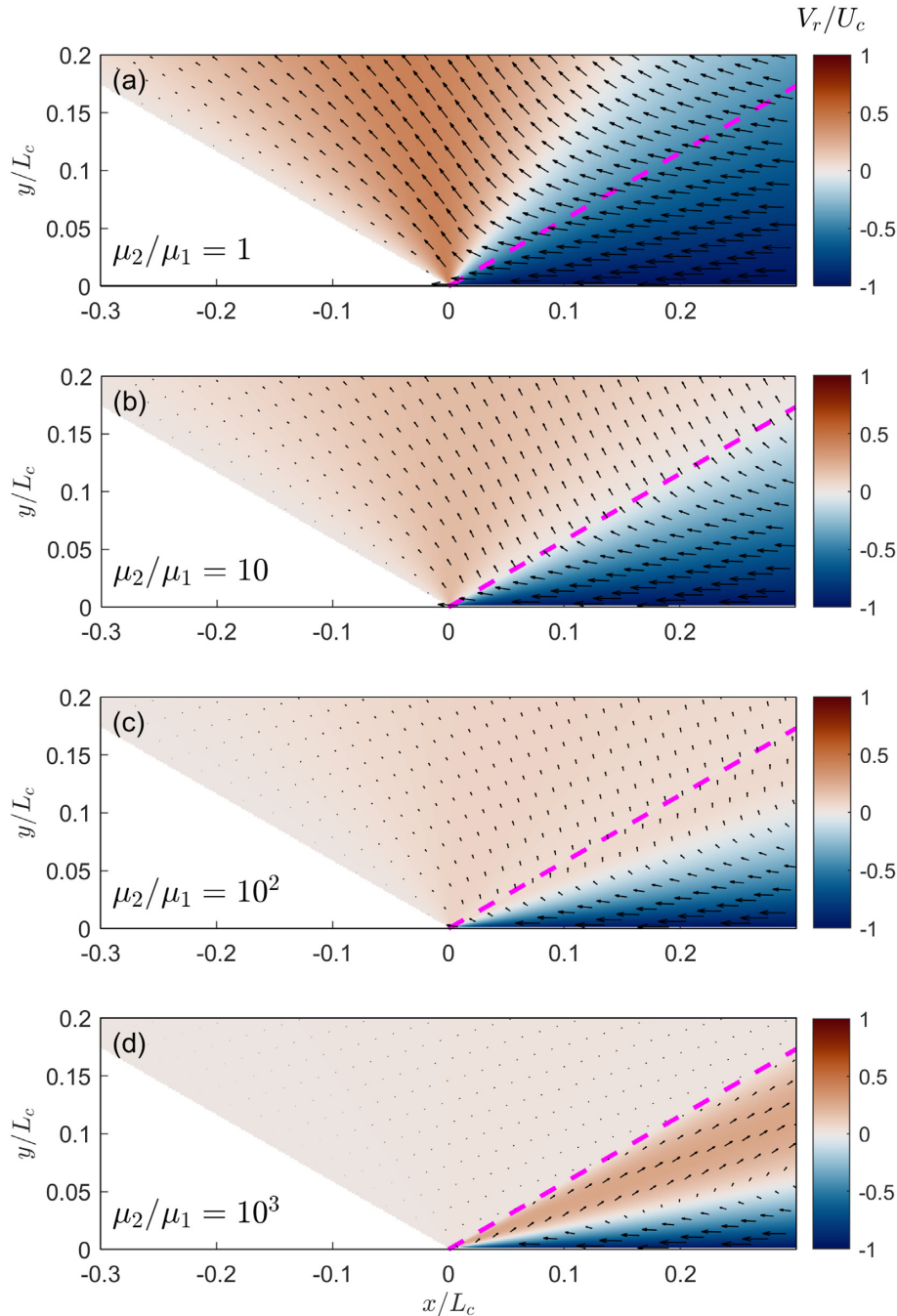


Figure 5. Velocity fields for a two-corner flow with $\theta_1 = 30^\circ$ and $\theta_2 = 150^\circ$, and with different viscosity ratios μ_2/μ_1 , ranging from 1 to 10^3 . The medial boundary is marked by a magenta dashed line. The grid of arrows shows the velocity field, and the colour map shows the magnitude of the radial velocity component, with positive values indicating flow away from the corner.

adjacent to the retro-boundary, but they are sufficient to cause the medial boundary to slowly migrate rearward with time. For all of the remaining examples, the velocity vectors adjacent to the medial boundary are zero or subparallel to that boundary, so the boundary is stable.

Fig. 7 shows examples for a very narrow pro-corner, where $\theta_1 = 10^\circ$. The first example (Fig. 7a) shows that pro-corner is unstable even with a very large viscosity ratio $\mu_2/\mu_1 = 10^3$. Also note that there is no backflow in this example. Instead, the high dynamic pressure inside the corner causes the medial boundary to migrate rearward. Fig. 7(b) shows that a viscosity ratio of $\mu_2/\mu_1 > 10^4$ is

able to maintain a stable pro-corner for this case. Thus, our overall conclusions from these examples are: 1) a stable pro-corner requires either a large viscosity ratio or an obtuse opening angle, and 2) backflow only occurs in a pro-corner with an acute opening angle and a very strong retro corner.

3.2 Dynamic pressure

One of the features of the analytical solution for the corner flow is the prediction of large dynamic pressure in the vicinity of the corner point. The dynamic pressure for the two-corner problem is given

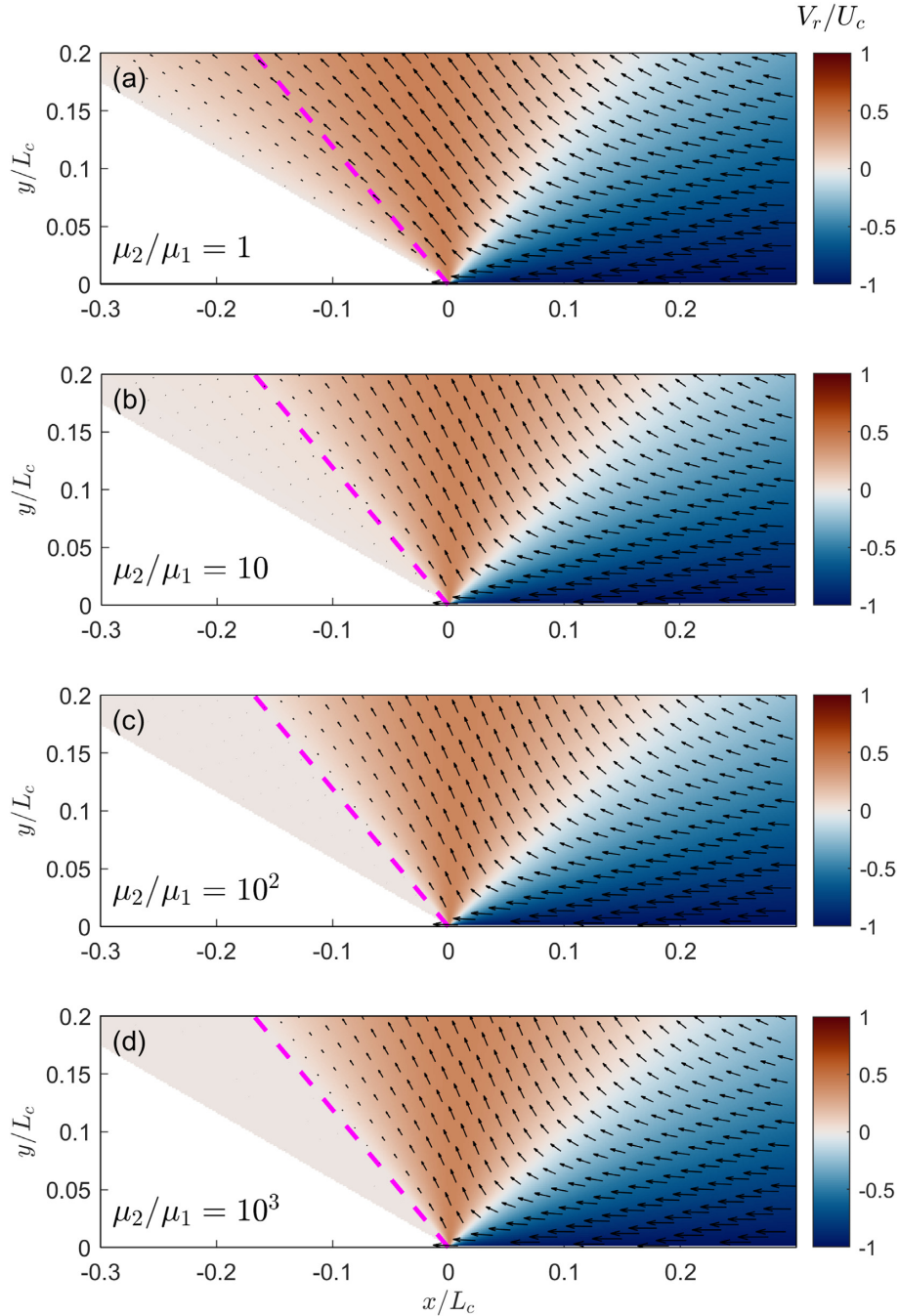


Figure 6. Velocity fields for a two-corner flow with $\theta_1 = 130^\circ$ and $\theta_2 = 150^\circ$. See Fig. 5 for further details.

by

$$P_d^k / \tau_c = 2 \left(\frac{\mu_k}{\mu_1} \right) \frac{C_k \cos(\theta) + D_k \sin(\theta)}{r/L_c}, \quad (11)$$

where k indicates the corner domain. Fig. 8 shows P_d fields for an acute pro-corner, with μ_2/μ_1 varying from 1 to 10^3 . Note that P_d is continuous across the medial boundary, as required by eq. 9c. Numerical simulations by van Keken *et al.* (2008) indicate that for a single narrow corner with rigid walls, the high in P_d is centered on the corner, and can reach values of 100 MPa. For our two-corner solutions, we find that the P_d high is influenced by the viscosity ratio. In all examples, the P_d high is offset rearward relative to the symmetric arrangement reported by van Keken *et al.* (2008).

The largest offset is found for the first example (Fig. 8a), which is equivalent to a single obtuse corner given that $\mu_2/\mu_1 = 1$, and the offset decreases with increasing μ_2/μ_1 . We speculate that it would become increasingly symmetric within an acute pro-corner as $\mu_2/\mu_1 \rightarrow \infty$, which approximates the case considered by van Keken *et al.* (2008).

Fig. 9(a) shows P_d in the pro-corner as a function of the radial distance along a section that follows the bisector of the pro-corner. Fig. 9(b) shows P_d at a fixed radial distance, $r/L_c = 1$ along the medial boundary, and as a function of varying pro-corner angles, θ_1 . These plots show that within a specific two-corner problem, P_d increases with decreasing r/L_c , and reaches a maximum at the corner point. And when considered as a function of configuration,

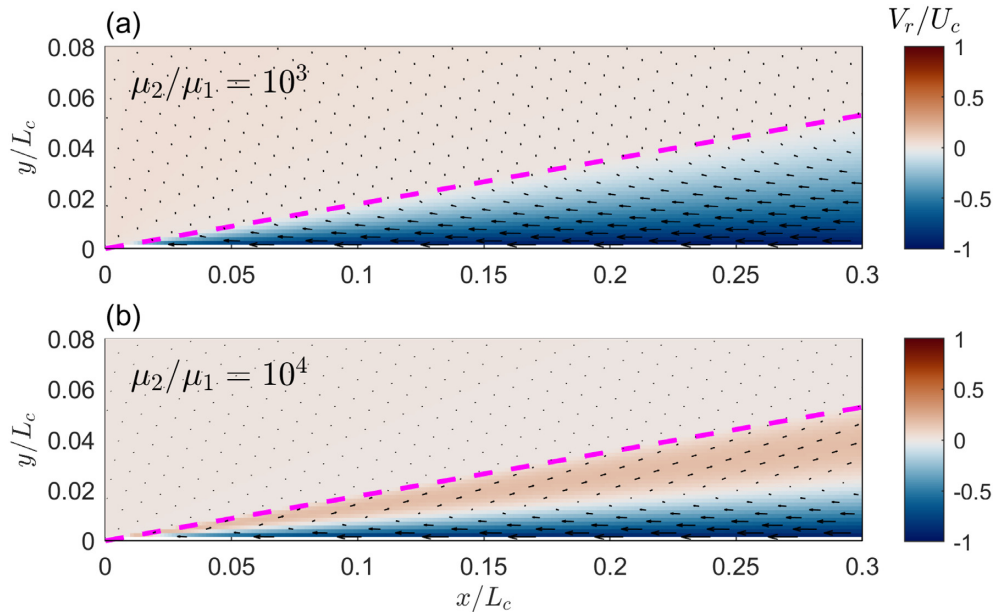


Figure 7. Velocity fields for a two-corner flow with $\theta_1 = 10^\circ$ and $\theta_2 = 150^\circ$ for viscosity ratios μ_2/μ_1 equal to 10^3 (a) and 10^4 (b). See Fig. 5 for further details.

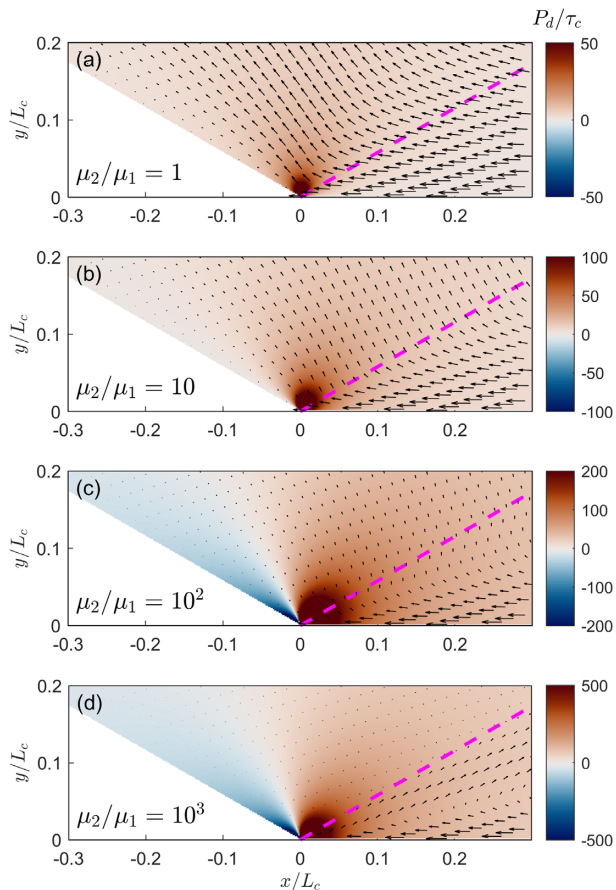


Figure 8. Dynamic pressure P_d field for a two-corner flow. The value of dynamic pressure has been normalized to the characteristic stress (τ_c). See Fig. 5 for further details.

the overall magnitude of P_d increases with increasing μ_2/μ_1 or with decreasing θ_1 .

3.3 Maintaining the corner geometry

A consequence of the analytical solution of the two-corner region (eqs 1–3) is that the circumferential velocity V_θ (i.e. normal to the radial direction) only depends on θ and otherwise remains constant as a function of r . This situation means that the motion of material points along a specified direction, θ , will include a rotation around the corner point that decreases in rate with increasing r (i.e. $\omega = V_\theta/r$ where $V_\theta(\theta) = \text{constant}$).

This feature of the analytical solution indicates that there will always be some circumferential shearing of the medial boundary. More specifically, V_θ at the medial boundary will increase with decreasing μ_2/μ_1 or decreasing θ_1 . As V_θ increases, so does the rearward migration and distortion of the medial boundary. In other words, increasing values of V_θ for the medial boundary indicate increasing instability for the pro-corner.

This conclusion is supported by numerical simulations in Fig. 10, which show the effect of this circumferential shearing after about $2t_c \approx 4$ Ma of flow (assuming characteristic values for U_c and L_c). The left and right set of examples are for acute pro-corners that start with opening angles $\theta_1 = 30^\circ$ and 10° , respectively. All of the examples show various developments of a large rearward-directed bulge in the medial boundary near the corner point. The examples show that pro-corner becomes more stable with an increasing viscosity ratio or an increasing opening angle.

Fig. 11 shows the normalized circumferential velocity, V_θ/U_c , as a function of θ_1 and μ_2/μ_1 , as determined from our two-corner analytical solution. The plot summarizes the conditions required to maintain a stable pro-corner. The white dashed line corresponds to $V_\theta/U_c = 2$ per cent, which we use to distinguish between stable and unstable corners.

3.4 Comparison to the England and Holland channel-flow model

An important aspect of the channel-flow models of England & Holland (1979) and Shreve & Cloos (1986) is that they account for

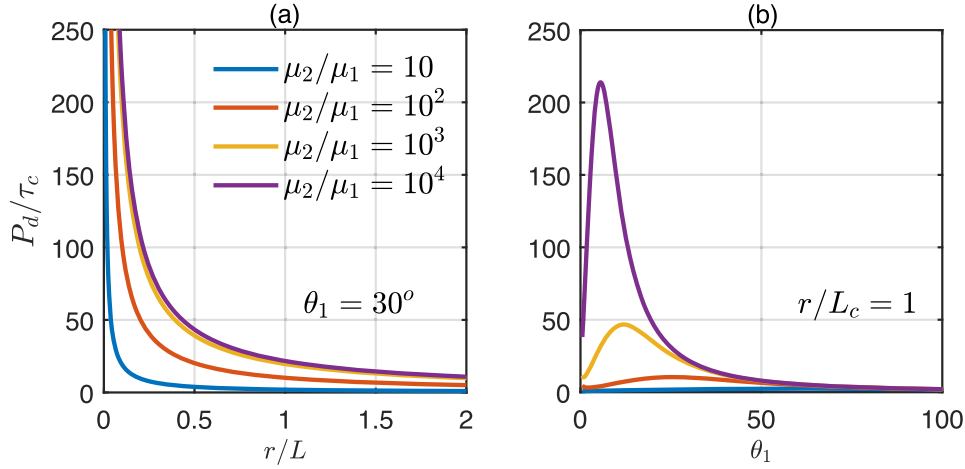


Figure 9. (a) Non-dimensional dynamic pressure P_d versus r for a pro-corner with an opening angle $\theta_1 = 30^\circ$. The values are for a transect along the centre of the pro-corner ($\theta = \theta_1/2$). (b) Non-dimensional dynamic pressure P_d at $r/L_c = 1$ on the medial boundary and as a function of difference opening angles, θ_1 , for the pro-corner.

buoyancy, an effect that is otherwise ignored in the corner-flow solutions considered above. Buoyancy becomes important when there is a significant contrast between the density of the material in the channel, and that of the adjacent walls ($\Delta\rho = \rho_c - \rho_w$). A positive density contrast would enhance downward flow within the channel, and a negative density contrast might activate a backflow in the upper part of the channel. We have seen above that backflow in forced corner flows is limited to the case of a stable narrow corner, and the driving force is a large dynamic pressure gradient created by the downward convergence of the flow. We show here that it is difficult to use the velocity fields associated with backflow to distinguish the driving force, whether buoyancy or dynamic pressure.

Here, we develop an approximation for a channel that has both (1) a dynamic pressure gradient parallel to the channel, as present in a narrow corner, and (2) a buoyancy gradient parallel to the channel, as is present in a buoyancy-driven channel flow. The layout for the comparison is shown in Figs 12(a) and (b). Two narrow corner geometries are considered, with opening angles of 5° and 15° .

The approximate relationship for the channel-parallel velocity V_x is developed in the Appendix. The final equation is

$$V_x = \frac{1}{2\mu} \left[\frac{dP_d}{dx} + \Delta\rho g_x \right] (y^2 - Hy) + U \left(\frac{y}{H} - 1 \right), \quad (12)$$

where μ is the viscosity of the material in the channel, H is the thickness of the channel, x is distance upward along the channel, and U is the entrainment velocity at the lower boundary of the flow. The gravitational acceleration vector is downward and oblique to the lower boundary (as expected for a dipping subduction zone). The constant g_x is the component of the gravitational acceleration parallel to the channel.

The similarity of the corner and channel velocity fields is indicated by the arrangement of the two terms in the square bracket of eq. (12). The first term, dP_d/dx , is the dynamic pressure gradient parallel to the channel. The second term, $\Delta\rho g_x$, is the buoyancy-related pressure gradient parallel to the channel. Eq. (12) shows that these two gradient terms have a similar influence on the V_x field.

This conclusion is illustrated by the results in Figs 12(c) and (d), which shows V_x/U_c across the channel for the two examples. The solid lines show the corner-flow solutions for V_x/U_c for the corner geometries in Figs 12(a) and (b). The plus and diamond symbols

show results for the channel-flow approximation (eq. 12) for V_x/U_c using a dynamic-pressure gradient and a buoyancy gradient, both oriented parallel to the channel. These examples demonstrate that the velocity fields alone are not sufficient to distinguish between a backflow driven by a dynamic pressure gradient or a buoyancy gradient, or a combination of the two.

4 DISCUSSION

An essential feature of the classic corner-flow model is the occurrence of backflow in acute corners (Fig. 1a). The backflow provides an interesting way in which HP/LT metamorphic rocks might be returned to the surface in subduction-zone settings. In the corner-flow model, the backflow is caused by convergence of the incoming flow. Our two-corner solution reveals that the maintenance of a stable pro-corner requires a large viscosity ratio ($\mu_2/\mu_1 \geq 10^3$, Fig. 5), and/or a relatively large opening angle ($\theta_1 > 90^\circ$, Figs 10 and 11). Conversely, a pro-corner with a narrow opening angle ($\theta_1 < 30^\circ$) and a viscosity ratio $\mu_2/\mu_1 < 10^2$ will evolve towards a larger opening angle, and the medial boundary will likely become distorted during this evolution. Nonetheless, we envision that as the pro-corner evolves towards this wider geometry, flow will cause material to move across the corner point, in a fashion similar to that shown for S-point models for wide wedges (Willett *et al.* 1993; Buck & Sokoutis 1994; Allemand & Lardeaux 1997; Medvedev 2002).

These observations suggest the following idea for evolution of subduction zones. When a subduction zone is first initiated, the resulting shear zone can be approximated by a pro-corner that has, by definition, a zero-opening angle, given that there has been no time to fill the corner with subducted sediment. We infer that most subduction zones lack the viscosity contrast required to sustain a narrow corner. Thus, the initially narrow pro-corner will evolve towards an opening angle that is in balance with the viscosity ratio μ_2/μ_1 for the subduction zone. More complex geodynamic models have also illustrated this behavior when an initial narrow subduction channel evolves into an orogenic wedge (Pfiffner *et al.* 2000). If our argument is correct, then the opening angle of the pro-corner at a mature subduction zone could be used to estimate an effective viscosity ratio, μ_2/μ_1 , for a real subduction zone.

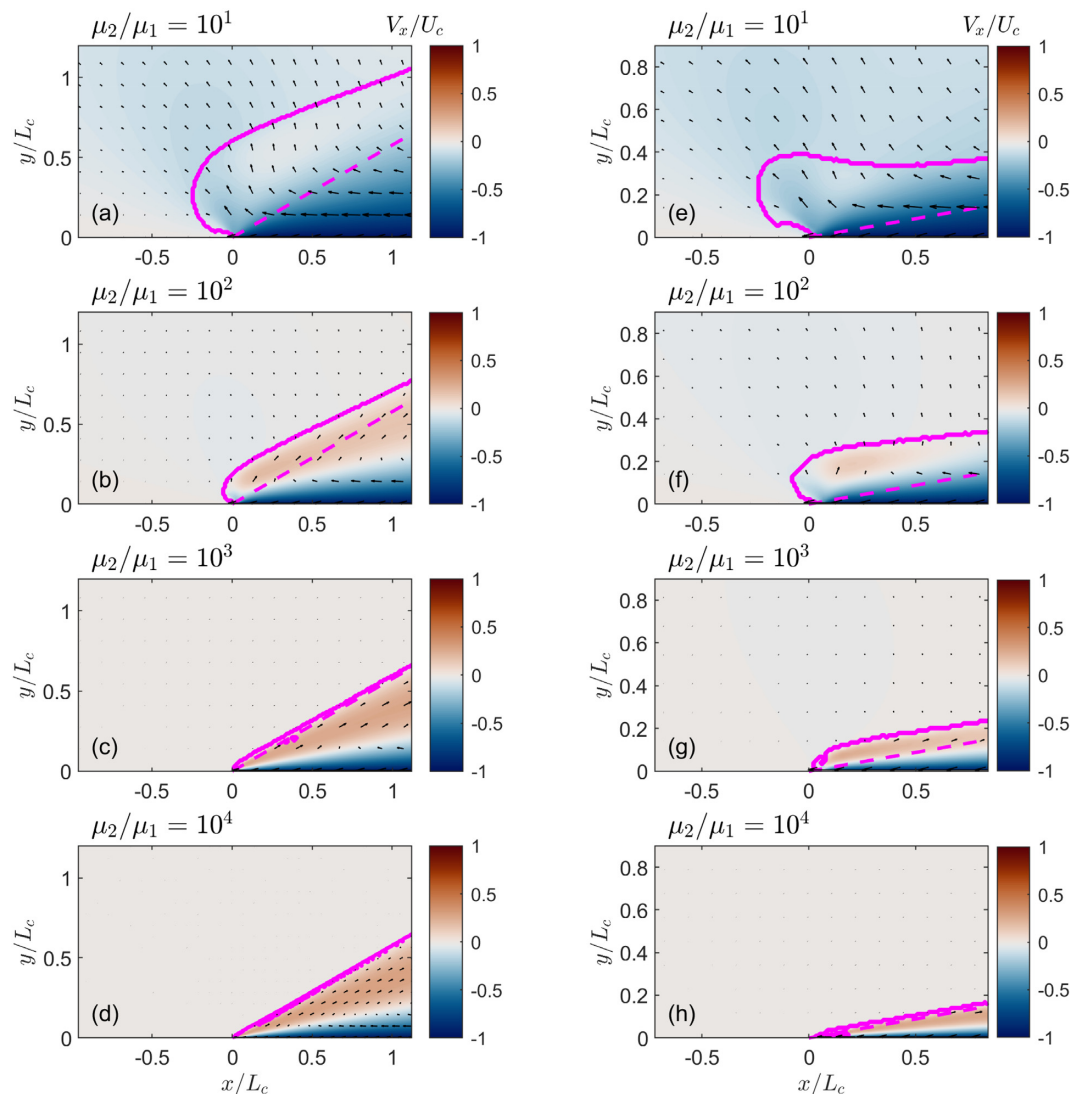


Figure 10. Numerical solutions showing the deformation of the medial boundary after a time interval of about $2t_c \approx 4$ Ma. The initial and final locations of the medial boundary are marked by dashed and solid magenta lines, respectively. Plots (a)–(d) focus on a pro-corner that starts with an acute geometry ($\theta_1 = 30^\circ$), and plots (e)–(h) focus on a pro-corner that starts with very narrow geometry ($\theta_1 = 10^\circ$). The colour map shows the non-dimensional horizontal component of velocity; positive values (brown colour) indicate backflow in the pro-corner. The calculations were done using the M2Di program (see details in Section 2.3).

Another interesting conclusion is that flow in a narrow channel or corner must be accompanied by a significant dynamic pressure high. This is an important issue in that metamorphic pressure is no longer a simple function of depth (Petrini & Podladchikov 2000; Moulas *et al.* 2013; Schmalholz & Podladchikov 2013; Bauville & Yamato 2021). A possible counter argument is that this dynamic pressure high might be reduced if the material inside the pro-corner were very weak. However, our analysis shows that an increase in the viscosity ratio (which is equivalent to ‘weakening’ the pro-corner materials) will cause an increase, not decrease, in the dynamic pressure high (Fig. 8). Thus, if the HP/LT blocks found in paleo-subduction settings like the Franciscan Complex were in fact exhumed within a narrow subduction channel, then the total pressure, P , must have been significantly greater than the lithostatic pressure, P_s . A rough estimate is that that P_d can reach values similar to P_s , which means that P would be about twice that of the

lithostatic pressure, P_s . As noted above, the blueschists and eclogites found in the Franciscan Complex have metamorphic pressures that range up to ~ 1.5 GPa (Wakabayashi 2015). If the dynamic pressure effect were zero, then these pressures would indicate maximum depths of 55 km (average density is taken as 2800 kg m^{-3}). If the dynamic pressure P_d achieves values comparable to the static pressure, P_s , then this maximum depth would be reduced by half, to ~ 27 km.

Another interesting feature of our corner flow solutions is that the dynamic pressure high extends across both the pro- and retro-corners. This result counters a common inference that HP/LT metamorphism is somehow related to strong shearing within the subduction zone. There are many examples, however, of HP/LT metamorphic rocks that show little to no deformation. To highlight this, we point to an eclogite sequence in the Zermatt-Saas-Fee zone of the Swiss Alps made famous by Bearth (1959). He discovered

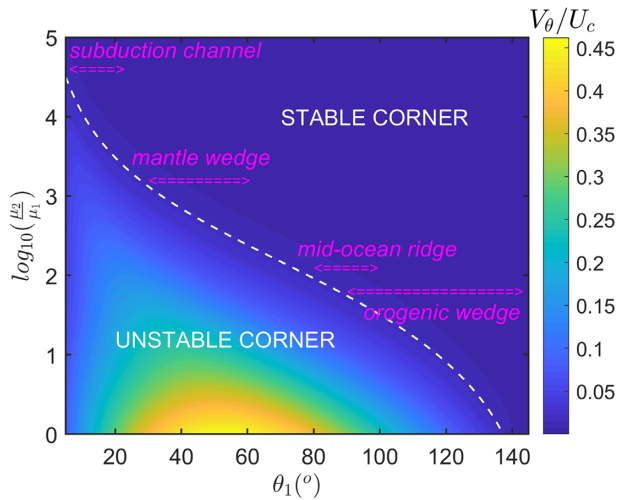


Figure 11. Non-dimensional circumferential velocity, V_{θ}/U_c , of the medial boundary as a function of the opening of the corner, θ_1 , and the logarithm of the viscosity ratio, μ_2/μ_1 . The white dashed line corresponds to a contour, where $V_{\theta}/U_c = 1/50$, and is used to distinguish stable and unstable pro-corners. The magenta labels show the viscosity ratio needed to sustain a stable corner for some representative tectonic settings on the Earth.

that this unit preserved the outlines of pillow basalts, and, in many places, the outlines were essentially undeformed (see fig. 1 in Ernst 2010, for a picture from this unit).

Our analysis overlooks the actual processes associated with accretion. This point is made clear by the fact that the accreted sediments of the pro-corner are already located above the subduction thrust. Accretion marks the transfer of material across the subduction thrust, and it is known to occur adjacent to the trench, as indicated by the term *offscraping* (or frontal accretion) and also by more deep-seated accretion, which called *underplating* (or basal accretion) (Sample & Fisher 1986). For our analysis, we have set $V_{\theta_0} = 0$ on the pro-boundary, which indicates that we have assumed that underplating is not a significant issue. However, our analysis can be easily extended to include underplating simply by adjusting V_{θ_0} to a positive value consistent with the rate of mass transfer into the pro-corner by this accretionary process. We infer that, with all other factors equal, the addition of an accretionary flux by underplating would further destabilize a narrow pro-corner, and it would probably affect the dynamic pressure as well. However, more work is needed to properly test these inferences.

Another result of this study is relevant for the case where the acute corner is approximated by a typical channel-flow geometry. The results provided by the two solutions (forced vs buoyant channel in Fig. 12) are indistinguishable and both solutions would predict the same velocity for a reasonable set of parameters. The similarity of the two solutions shows, in fact, that structural observations alone are probably not sufficient to distinguish between a buoyancy-driven backflow or a pressure-driven backflow.

At this point, we would like to emphasize that the most important factor for the maintenance of the corner geometry and the generation of backflow is the viscosity ratio between the pro-corner and the overriding plate. Large viscosity ratios can be expected in nature as a consequence of the different lithologies and the variety of physical conditions (temperature, fugacity of volatiles, lithology, etc.). However, there are two competing phenomena that occur in association with metamorphism during subduction. On the one hand, the subduction of material, and the associated pressure and temperature

increase leads to devolatilization and densification within the pro-corner. On the other hand, this devolatilization might also lead to the hydration and weakening of the overriding plate. For both cases, the viscosity ratio decreases and the pro-corner would become less stable and more transient.

Finally, we end with a comment about *mélanges*. In Cloos' (1982) view, *mélange* formation is intrinsically related to corner flow, as emphasized by his term 'flow *mélange*'. However, Cloos (1982) also recognized that the mixing observed in *mélanges* cannot be directly related to corner flow since the velocity field is laminar (low Reynolds number), and not turbulent. Therefore, he proposed that the mixing was caused by plucking of dense HP/LT blocks from the hanging wall, which then settled at variable rates through the actively flowing material in the pro-corner. The idea of blocks dispersing by 'Stokes settling' within an active corner flow is entirely plausible. However, our analysis indicates that the maintenance of active flow in a narrow corner requires that the material in the pro-corner is exceptionally weak, or the upper plate (i.e. the retro-corner) is exceptionally strong. This requirement provides an approach to test the viability of the subduction channel idea.

5 CONCLUSIONS

A new analytical solution for the study of viscous incompressible flow in corner regions has been developed. The analytical solution shows that the activation of a strong backflow requires a narrow corner, which is the expected situation shortly after initiation of a subduction zone. The convergence of accreted materials into a narrow pro-corner creates a large dynamic pressure. As such, HP/LT metamorphism can occur in such settings at depths much shallower, by as much as a factor of two, than that predicted by the common assumption that the total pressure is equal static pressure. Our inference is that the overlying retro-corner is generally not strong enough to sustain a narrow pro-corner, which means that the medial boundary above the pro-corner will migrate rearward into the overriding plate. Thus, with time, an initially narrow pro-corner will evolve to an obtuse geometry. This wider configuration is consistent with the observation of widespread uplift and deformation across the forearc high at most actively accreting subduction zones.

Much of the discussion about accretion, HP/LT metamorphism, and exhumation at subduction zones is framed by the idea of a confined flow inside a narrow corner or a thin channel. The basic forcing for the flow is thought to be entrainment of accreted materials that overlies the subducting plate. The corner-flow problem is based solely on this kinematic forcing. The channel flow problem includes both kinematic and buoyancy forcing. Some authors have argued that structures in the field may be able to distinguish between these two kinds of forcings. We show that, in fact, the velocity fields associated with kinematic and buoyancy forcings are remarkably similar, and thus would be difficult to diagnosis by structural observations alone.

ACKNOWLEDGEMENTS

We acknowledge Jenny Collier for the editorial handling and the reviewers (D. Schlaphorst & A. Bauville) for their constructive comments that allowed us to improve the manuscript. EM acknowledges the Johannes Gutenberg University Mainz for financial support. MTB acknowledges support from NSF EAR-1650313. JDVH and SMS were supported by SNF grant No. 200021_165756. The initial discussions related to this paper took part while EM was

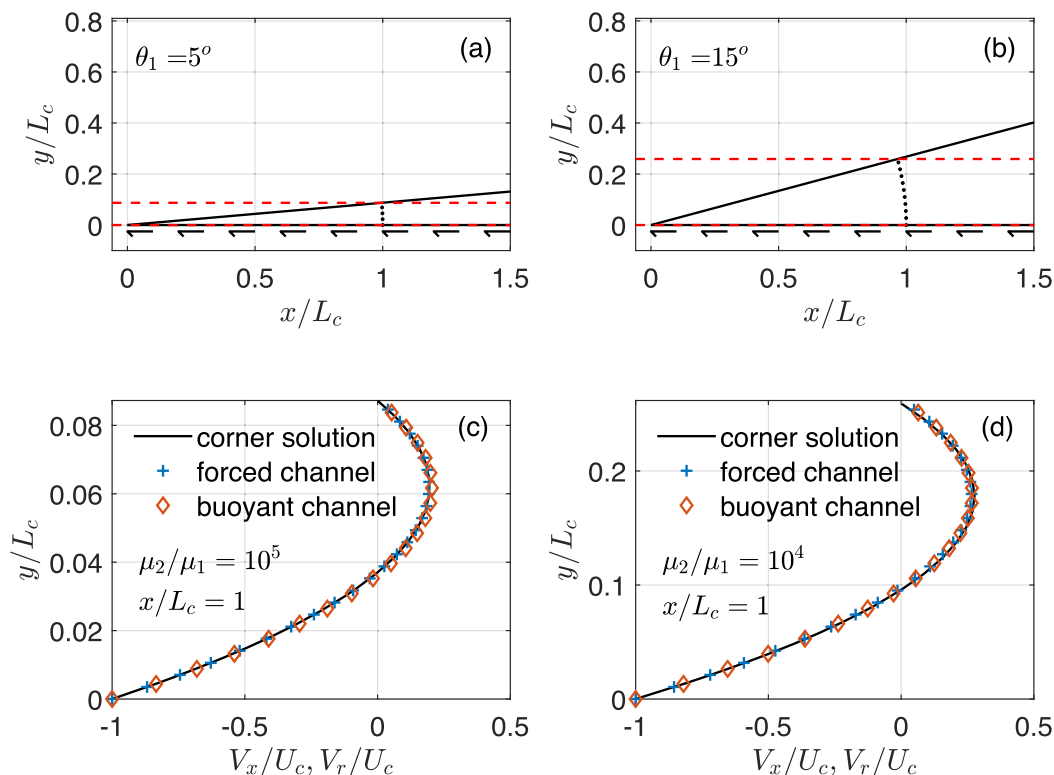


Figure 12. Comparisons of narrow corner flows with forced flows and buoyant flows in channels with similar equivalent thicknesses. Panels (a) and (c) show results for a very narrow case ($\theta_1 = 5^\circ$), and panels (b) and (d) show results for a narrow case ($\theta_1 = 15^\circ$). The viscosity ratios are adjusted to ensure a stable corner. Panels (a) and (b) show the layout for the corner and the equivalent channel for each example. The lower boundary corresponds to the top of the subducting plate, and the barbed arrows indicate the direction for entrainment at the base of the flow field. Panels (c) and (d) show various estimates for V_x/U_c , as measured across the corner or channel at $x/L_c = 1$. The solid lines show the V_x/U_c profiles for the corner-flow solutions, and the symbols show the V_x/U_c profiles as estimated by eq. (12) for specified along-channel gradients in pressure (plus symbols) and buoyancy (diamond symbols). The rest of the model parameters are: the density difference is -300 kg m^{-3} , velocity is 5 cm a^{-1} , and the channel viscosities are $\sim 1.5 \times 10^{17}$ and $1.2 \times 10^{18} \text{ Pa s}$ for (a) and (b), respectively.

visiting MTB at Yale University. Susan Monsen is acknowledged for her hospitality and patience during our long discussions. MTB thanks Kurt Stüwe for a 2019 field trip introduction to the Austria eclogites. Thibault Duret and Ludovic Räss are acknowledged for help related to the adaptation of the M2Di solver for the corner geometry.

DATA AVAILABILITY

wxMaxima and MATLAB scripts are provided in the Supporting Information. These files can be used for the calculation and visualization of the analytical solution presented in this work.

REFERENCES

- Adamuszek, M., Dabrowski, M. & Schmid, D.W., 2016. Folder: a numerical tool to simulate the development of structures in layered media, *J. Struct. Geol.*, **84**, 85–101.
- Allemand, P. & Lardeaux, J.-M., 1997. Strain partitioning and metamorphism in a deformable orogenic wedge: application to the Alpine belt, *Tectonophysics*, **280**, 157–169.
- Ampferer, O. & Hammer, W., 1911. *Geologischer Querschnitt durch die Ostalpen vom Allgäu zum Gardasee*, Jahrbuch der Kaiserlich-Königlichen Geologischen Reichsanstalt, Vol. 61, pp. 532–710, Geologischen Reichsanstalt.
- Anderson, D.M. & Davis, S.H., 1993. Two-fluid viscous flow in a corner, *J. Fluid Mech.*, **257**, 1–31.

- Argand, E., 1916. Sur l'arc des Alpes Occidentales, *Eclogae Geol. Helvetiae*, **14**, 145–191.
- Argand, E., 1924. Des Alpes et de l'Afrique, *Bull. Soc. Vaudoise Sci. Nat.*, **55**, 233–236.
- Batchelor, G.K., 1967. *An Introduction to Fluid Dynamics*, Cambridge Univ. Press.
- Bauville, A. & Yamato, P., 2021. Pressure-to-depth conversion models for metamorphic rocks: derivation and applications, *Geochem. Geophys. Geosyst.*, **22**, e2020GC009280.
- Bearth, P., 1959. Über Eklogite, Glaukophanschiefer und metamorphe Pillowlaven, *Schweiz. Mineral. Petrogr. Mitteilungen*, **39**, 267–286.
- Baumont, C. & Quinlan, G., 1994. A geodynamic framework for interpreting crustal-scale seismic-reflectivity patterns in compressional orogens, *Geophys. J. Int.*, **116**, 754–783.
- Beuchert, M.J. & Podladchikov, Y.Y., 2010. Viscoelastic mantle convection and lithospheric stresses, *Geophys. J. Int.*, **183**, 35–63.
- Bird, P., 2003. An updated digital model of plate boundaries, *Geochem. Geophys. Geosyst.*, **4**, doi:10.1029/2001GC000252.
- Buck, W.R. & Sokoutis, D., 1994. Analogue model of gravitational collapse and surface extension during continental convergence, *Nature*, **369**, 737–740.
- Camerlengi, A. & Pini, G.A., 2009. Mud volcanoes, olistostromes and Argille scagliose in the Mediterranean region, *Sedimentology*, **56**, 319–365.
- Chang, C.P., Angelier, J., Huang, C.Y. & Liu, C.S., 2001. Structural evolution and significance of a mélange in a collision belt: the Lichi Mélange and the Taiwan arc–continent collision, *Geol. Mag.*, **138**, 633–651.

- Claussmann, B. *et al.*, 2021. Shelf-derived mass-transport deposits: origin and significance in the stratigraphic development of trench-slope basins, *N.Z. J. Geol. Geophys.*, 1–36, doi:10.1080/00288306.2021.1918729.
- Cloos, M., 1982. Flow melanges: numerical modeling and geologic constraints on their origin in the Franciscan subduction complex, California, *Bull. geol. Soc. Am.*, **93**, 330–345.
- Cloos, M., 1984. Flow melanges and the structural evolution of accretionary wedges, in *Melanges: Their Nature, Origin, and Significance*, Vol. 198, ed. Raymond, L.A., Geological Society of America.
- Cloos, M. & Shreve, R.L., 1988a. Subduction-channel model of prism accretion, melange formation, sediment subduction, and subduction erosion at convergent plate margins: 2. Implications and discussion, *Pure appl. Geophys.*, **128**, 501–545.
- Cloos, M. & Shreve, R.L., 1988b. Subduction-channel model of prism accretion, melange formation, sediment subduction, and subduction erosion at convergent plate margins: 1. Background and description, *Pure appl. Geophys.*, **128**, 455–500.
- Cowan, D.S., 1985. Structural styles in Mesozoic and Cenozoic mélanges in the western Cordillera of North America, *Bull. geol. Soc. Am.*, **96**, 451–462.
- Cowan, D.S. & Silling, R.M., 1978. A dynamic, scaled model of accretion at trenches and its implications for the tectonic evolution of subduction complexes, *J. geophys. Res.*, **83**, 5389–5396.
- Dean, W.R. & Montagnon, P.E., 1949. On the steady motion of viscous liquid in a corner, *Math. Proc. Camb. Phil. Soc.*, **45**, 389–394.
- Duret, T., May, D.A., Gerya, T.V. & Tackley, P.J., 2011. Discretization errors and free surface stabilization in the finite difference and marker-in-cell method for applied geodynamics: a numerical study, *Geochem. Geophys. Geosyst.*, **12**, doi:10.1029/2011GC003567.
- Emerman, S.H. & Turcotte, D.L., 1983. A fluid model for the shape of accretionary wedges, *Earth planet. Sci. Lett.*, **63**, 379–384.
- England, P. & Wilkins, C., 2004. A simple analytical approximation to the temperature structure in subduction zones, *Geophys. J. Int.*, **159**, 1138–1154.
- England, P.C. & Holland, T.J.B., 1979. Archimedes and the Tauern eclogites: the role of buoyancy in the preservation of exotic eclogite blocks, *Earth planet. Sci. Lett.*, **44**, 287–294.
- Ernst, W.G., 2010. Subduction zone metamorphism—pioneering contributions from the Alps, *Int. Geol. Rev.*, **52**, 1021–1039.
- Fletcher, R.C., 1977. Folding of a single viscous layer: exact infinitesimal-amplitude solution, *Tectonophysics*, **39**, 593–606.
- Gerya, T.V., Stöckhert, B. & Perchuk, A.L., 2002. Exhumation of high-pressure metamorphic rocks in a subduction channel: a numerical simulation, *Tectonics*, **21**, 6–1–6–19.
- Henriksen, P. & Hassager, O., 1989. Corner flow of power law fluids, *J. Rheol.*, **33**, 865–879.
- Jamieson, R.A. & Beaumont, C., 2013. On the origin of orogens, *Bull. geol. Soc. Am.*, **125**, 1671–1702.
- Krohe, A., 2017. The Franciscan Complex (California, USA)—the model case for return-flow in a subduction channel put to the test, *Gondwana Res.*, **45**, 282–307.
- Landau, L.D. & Lifshitz, E.M., 1987. *Course of Theoretical Physics, Vol. 6, Fluid Mechanics*, 2nd edn, Pergamon.
- Lundberg, N. & Moore, J.C., 1986. Macroscopic structural features in Deep Sea Drilling Project cores from forearc regions, in *Structural Fabrics in Deep Sea Drilling Project Cores From Forearcs*, Vol. 166, ed. Moore, J.C., Geological Society of America.
- Mancktelow, N.S., 1995. Nonlithostatic pressure during sediment subduction and the development and exhumation of high pressure metamorphic rocks, *J. geophys. Res.*, **100**, 571–583.
- McKenzie, D.P., 1969. Speculations on the consequences and causes of plate motions, *Geophys. J. R. astr. Soc.*, **18**, 1–32.
- Medvedev, S., 2002. Mechanics of viscous wedges: modeling by analytical and numerical approaches, *J. geophys. Res.*, **107**, ETG 9–1–ETG 9–15.
- Moffatt, H.K., 1964. Viscous and resistive eddies near a sharp corner, *J. Fluid Mech.*, **18**, 1–18.
- Moulas, E., Burg, J.-P. & Podladchikov, Y., 2014. Stress field associated with elliptical inclusions in a deforming matrix: mathematical model and implications for tectonic overpressure in the lithosphere, *Tectonophysics*, **631**, 37–49.
- Moulas, E. & Schmalholz, S.M., 2020. The importance of interfacial instability for viscous folding in mechanically heterogeneous layers, *Geol. Soc. Lond. Spec. Publ.*, **487**, 45–58.
- Moulas, E., Podladchikov, Y.Y., Aranovich, L.Y. & Kostopoulos, D.K., 2013. The problem of depth in geology: when pressure does not translate into depth, *Petrology*, **21**, 527–538.
- Moulas, E., Schmalholz, S.M., Podladchikov, Y., Tajčmanová, L., Kostopoulos, D. & Baumgartner, L., 2019. Relation between mean stress, thermodynamic, and lithostatic pressure, *J. Metamorph. Geol.*, **37**, 1–14.
- Page, B.M. & Suppe, J., 1981. The Pliocene Lichi melange of Taiwan; its plate-tectonic and olistostromal origin, *Am. J. Sci.*, **281**, 193–227.
- Pazzaglia, F.J. & Brandon, M.T., 2001. A fluvial record of long-term steady-state uplift and erosion across the Cascadia Forearc High, Western Washington State, *Am. J. Sci.*, **301**, 385–431.
- Petrini, K. & Podladchikov, Y., 2000. Lithospheric pressure–depth relationship in compressive regions of thickened crust, *J. Metamorph. Geol.*, **18**, 67–77.
- Pfiffner, O.A., Ellis, S. & Beaumont, C., 2000. Collision tectonics in the Swiss Alps: insight from geodynamic modeling, *Tectonics*, **19**, 1065–1094.
- Pollard, D.D. & Fletcher, R.C., 2005. *Fundamentals of Structural Geology*, Cambridge Univ. Press.
- Raimbourg, H. & Kimura, G., 2008. Non-lithostatic pressure in subduction zones, *Earth planet. Sci. Lett.*, **274**, 414–422.
- Räss, L., Duret, T., Podladchikov, Y.Y. & Schmalholz, S.M., 2017. M2Di: concise and efficient MATLAB 2-D Stokes solvers using the finite difference method, *Geochem. Geophys. Geosyst.*, **18**, 755–768.
- Ribe, N.M., 1989. Mantle flow induced by back arc spreading, *Geophys. J. Int.*, **98**, 85–91.
- Ribe, N.M., 2015. Analytical approaches to mantle dynamics, in *Treatise on Geophysics*, Vol. 7, pp. 145–196, ed. Bercovici, D., Elsevier.
- Ribe, N.M., 2018. *Theoretical Mantle Dynamics*, 1st edn, Cambridge Univ. Press.
- Ribe, N.M. & Xu, B., 2020. Subduction of non-Newtonian plates: thin-sheet dynamics of slab necking and break-off, *Geophys. J. Int.*, **220**, 910–927.
- Riedler, J. & Schneider, W., 1983. Viscous flow in corner regions with a moving wall and leakage of fluid, *Acta Mech.*, **48**, 95–102.
- Ring, U. & Brandon, M.T., 1999. Ductile deformation and mass loss in the Franciscan Subduction Complex: implications for exhumation processes in accretionary wedges, *Geol. Soc. Lond. Spec. Publ.*, **154**, 55, doi:10.1144/GSL.SP.1999.154.01.03.
- Sample, J.C. & Fisher, D.M., 1986. Duplex accretion and underplating in an ancient accretionary complex, Kodiak Islands, Alaska, *Geology*, **14**, 160–163.
- Schellart, W.P., 2008. Kinematics and flow patterns in deep mantle and upper mantle subduction models: influence of the mantle depth and slab to mantle viscosity ratio, *Geochem. Geophys. Geosyst.*, **9**, doi:10.1029/2007GC001656.
- Schmalholz, S.M., 2011. A simple analytical solution for slab detachment, *Earth planet. Sci. Lett.*, **304**, 45–54.
- Schmalholz, S.M. & Podladchikov, Y.Y., 2013. Tectonic overpressure in weak crustal-scale shear zones and implications for the exhumation of high-pressure rocks, *Geophys. Res. Lett.*, **40**, 1984–1988.
- Schmid, D.W. & Podladchikov, Y.Y., 2003. Analytical solutions for deformable elliptical inclusions in general shear, *Geophys. J. Int.*, **155**, 269–288.
- Shreve, R.L. & Cloos, M., 1986. Dynamics of sediment subduction, melange formation, and prism accretion, *J. geophys. Res.*, **91**, 10 229–10 245.
- Spiegelman, M. & McKenzie, D., 1987. Simple 2-D models for melt extraction at mid-ocean ridges and island arcs, *Earth planet. Sci. Lett.*, **83**, 137–152.
- Sprittles, J.E. & Shikhmurzaev, Y.D., 2011. Viscous flow in domains with corners: numerical artifacts, their origin and removal, *Comput. Methods Appl. Mech. Eng.*, **200**, 1087–1099.
- Stevenson, D.J. & Turner, J.S., 1977. Angle of subduction, *Nature*, **270**, 334–336.

- Tovish, A., Schubert, G. & Luyendyk, B.P., 1978. Mantle flow pressure and the angle of subduction: non-Newtonian corner flows, *J. geophys. Res.*, **83**, 5892–5898.
- Turcotte, D.L. & Schubert, G., 2014. *Geodynamics*, 3rd edn, Cambridge Univ. Press.
- van Keken, P.E. *et al.*, 2008. A community benchmark for subduction zone modeling, *Phys. Earth Planet. Inter.*, **171**, 187–197.
- Wakabayashi, J., 2015. Anatomy of a subduction complex: architecture of the Franciscan Complex, California, at multiple length and time scales, *Int. Geol. Rev.*, **57**, 669–746.
- Willett, S., Beaumont, C. & Fullsack, P., 1993. Mechanical model for the tectonics of doubly vergent compressional orogens, *Geology*, **21**, 371–374.

SUPPORTING INFORMATION

Supplementary data are available at [GJI](https://doi.org/10.1017/gji.2021.15766309899) online.

Electronic_Supplementary_Material.zip

Please note: Oxford University Press is not responsible for the content or functionality of any supporting materials supplied by the authors. Any queries (other than missing material) should be directed to the corresponding author for the paper.

APPENDIX: COMPARISON OF CORNER AND CHANNEL FLOW

Here, we derive the equations that are used to compare a channel flow between two parallel walls and a corner flow with a small angle. The channel flow is derived from the equations for slow incompressible viscous flow (Landau & Lifshitz 1987, p. 52; Turcotte & Schubert 2014, p. 270). The coordinates are Cartesian with x is directed upward and parallel to the channel ($\theta = \theta_0$) and y is perpendicular to the channel ($\theta = \theta_0 + 90^\circ$). The governing equation for the total pressure P (equal to the negative mean stress) is

$$\mu \frac{d^2 V_x}{dy^2} = \frac{dP}{dx} - \rho g_x, \quad (\text{A1})$$

where V_x is the channel-parallel velocity, ρ and μ are the density and viscosity of the material in the channel and g_x is the x -component of gravitational acceleration (parallel to the channel). Eq. (A1) is modified by separating the total pressure P into static P_s and dynamic P_d components, and then simplifying, which give

$$\mu \frac{d^2 V_x}{dy^2} = \frac{dP_d}{dx} + \Delta\rho g_x, \quad (\text{A2})$$

where $\Delta\rho = \rho_c - \rho_w$ is the density difference between the channel material and the surrounding wall rock. The solution is

$$V_x = \frac{1}{2\mu} \left(\frac{dP_d}{dx} + \Delta\rho g_x \right) y^2 + c_1 y + c_2, \quad (\text{A3})$$

where c_1 and c_2 are integration constants determined by the boundary conditions. By setting $V_x = -U$ at $y = 0$ and $V_x = 0$ at $y = H$, we obtain

$$c_1 = \frac{U}{H} - \frac{1}{2\mu} \left(\frac{dP_d}{dx} + \Delta\rho g_x \right) H, \quad (\text{A4a})$$

and

$$c_2 = -U. \quad (\text{A4b})$$

We assume that, for the region of interest, the dynamic pressure gradient, dP_d/dx , is approximately constant and the channel-parallel velocity gradient, dV_x/dx , is approximately zero. A constant pressure gradient is a reasonable assumption for regions away from the corner ($r/L_c > 1$; see also Fig. 9a).

Eqs (A3) and (A4) can now be used to approximate the radial component in a narrow corner, as shown in Fig. 12. Inspection of eq. (A3) reveals that there are two quadratic terms related to the backflow component of the velocity field. The first is related to P_d , which is caused by downward convergence associated with the forced flow, and the second is related to the buoyancy forces associated with the density contrast between the channel and surrounding walls. In other words, eq. (A3) is a more general form of the channel-flow solution, and is also similar to the general solutions developed by Shreve & Cloos (1986) and Mancktelow (1995).

The corner-flow solution is represented by setting $\Delta\rho = 0$, which means that buoyancy effects are turned off. Eqs (A3) and (A4) indicate that in the absence of buoyancy forces, the only way to drive a backflow is by a negative gradient in the dynamic pressure dP_d/dx , as needed to drive the flow upward. We can now consider a narrow corner region (with $\theta_2 = 150^\circ$) at a location $x/L_c = 1$ (x coincides with the radial direction, r , as in Figs 12a and b). The pressure gradient can be approximated at the limit of small angles ($\cos(\theta_1) \approx 1$, $\sin(\theta_1) \approx 0$). Thus, the dynamic pressure gradient within the corner can be approximated from eq. (11) as

$$\frac{dP_d}{dr} \approx -2 \frac{C_1}{r^2} \tau_c L_c, \quad (\text{A5})$$

where C_1 is an integration constant from the two-corner analytical solution. By inserting the result of eq (A5) into eqs (A3) and (A4), we obtain the solution shown in Figs 12(c) and (d) (forced channel).